ORNL/TM-2017/228

# High-Temperature Steam Oxidation Testing of Select Advanced Replacement Alloys for Potential Core Internals

Lizhen Tan
Bruce A. Pint

**May 19, 2017**

**OAK RIDGE NATIONAL LABORATORY**

ORNL/TM-2017/228

Light Water Reactor Sustainability (LWRS) Program
M3LW-17OR0406023

# HIGH-TEMPERATURE STEM OXIDATION TESTING OF SELECT ADVANCED REPLACEMENT ALLOYS FOR POTENTIAL CORE INTERNALS

Lizhen Tan, Bruce A. Pint

Date Published: May 19, 2017

**CONTENTS**

# LIST OF FIGURES

**Figure**                                                                                                                    **Page**

# LIST OF TABLES

**Table**                                                                                                         **Page**

# ACKNOWLEDGMENTS

# EXECUTIVE SUMMARY

Life extension of the existing nuclear reactors imposes irradiation of high fluences to structural materials, resulting in significant challenges to the traditional reactor materials such as type 304 and 316 stainless steels. Advanced alloys with superior radiation resistance will increase safety margins, design flexibility, and economics for not only the life extension of the existing fleet but also new builds with advanced reactor designs. The Electric Power Research Institute (EPRI) teamed up with Department of Energy (DOE) to initiate the Advanced Radiation Resistant Materials (ARRM) program, aiming to develop and test degradation resistant alloys from current commercial alloy specifications by 2021 to a new advanced alloy with superior degradation resistance in light water reactor (LWR)-relevant environments by 2024.

Oxidation resistance in water environment is one of the fundamental properties required for core internal materials. High-temperature steam oxidation tests are not only an accelerated life testing method to uncover potential failure modes in a short period of time, but also an approach to evaluate materials' resistance to accidental scenarios. According to the candidate alloys selected under the ARRM program, a total of fourteen commercial and custom fabricated alloys, procured from a variety of vendors or producers, were tested in this work. The alloys include three ferritic steels (Grade 92, Alloy 439, and an oxide-dispersion-strengthened alloy 14YWT), three austenitic stainless steels (316L, 310, and 800), seven Ni-base superalloys (X750, 725, C22, 690, 625, 625 direct-aging, and 625-plus), and one zirconium alloy (Zr–2.5Nb). Candidate Ni-base superalloy 718 was procured too late to be included in the tests. Among the fourteen alloys, 316L and X750 are served as reference alloys for low- and high-strength alloys, respectively.

Coupons were prepared from the fourteen candidate alloys and exposed to 1 bar full steam with ~10 part-per-billion oxygen content at 600 and 650°C. The coupons were weighed at 500-h intervals with a targeted exposure time of 5,000 h. Alloy Zr–2.5Nb was only tested one cycle (500 h) because of the exceptional weight gains and extensive oxide scales formed on the coupons. The tests of 310 and X750 are still in progress because of the later availability of the two alloys compared to the other twelve alloys. This report summarizes the completed test results of Grade 92, 439, 14YWT, 316L, 800, 725, C22, 690, 625, 625 direct-aging, 625-plus, and Zr-2.5Nb, together with the preliminary test results of 310 and X750.

Unlike the excessive oxidation of Zr–2.5Nb, ferric steels Grade 92, Alloy 439, and 14YWT showed moderate weight gains in a descending order, which are believed to be primarily determined by their chromium content (9, 18, and 14Cr, respectively) and grain sizes (~40, ~50, and ~0.8 µm, respectively). Oxide scale characterization by optical microscopy revealed pores in the outer oxide layer of the ferritic steels, which caused some scale exfoliation. Significant weight losses with extensive scale exfoliation were observed in 316L. The significantly increased amounts of chromium and nickel in 310, 800, and the Ni-base superalloys led to small or negligible weight changes. Among the Ni-base superalloys, C22 seems to have the worst oxidation resistance, which exhibited the most weight losses at 600°C and unstable weight gains at 650°C, likely attributable to the formation of volatile oxides induced by its high Mo content. The corrosion rates of the candidate alloys can be approximately interpreted by their Cr, Ni and Fe content. Simplified thermodynamics analyses of the alloy oxidation provided reasonable indications for the constituents of oxide scales formed on the alloys and explanations for the porosity and exfoliation phenomena because of the nature of specific types of oxides.

# 1. INTRODUCTION

Nuclear power currently provides a significant fraction of the United States' non-carbon emitting power generation. In future years, nuclear power must continue to generate a significant portion of the nation's electricity to meet the growing electricity demand, clean energy goals, and to ensure energy independence. New reactors will be an essential part of the expansion of nuclear power. However, given limits on new builds imposed by economics and industrial capacity, the extended service of the existing fleets will also be required.

Nuclear reactors present a very harsh environment for components service. Components within a reactor core must tolerate high temperatures, water, stress, vibration, and an intense neutron field. With the nominal irradiation temperature of ~290°C in light water reactors (LWRs), actual component temperatures range from 270°C to 370°C depending on the relative position of the component within the reactor core and relative amounts of cooling and gamma heating. Degradation of materials in this environment can lead to reduced performance, and in some cases, sudden failure.

Extending the service life of a reactor will increase the total neutron fluence to each component and may result in radiation-induced effects not yet observed in LWR conditions, although this form of degradation has been observed in fast reactor conditions. Radiation-induced processes must be carefully considered for higher fluences, particularly the influence of radiation-induced segregation (RIS), swelling, and/or precipitation on embrittlement. Neutron irradiation field can produce large property and dimensional changes in materials. For LWRs, high-temperature embrittlement and creep are not common problems due to the lower reactor temperature. However, radiation embrittlement, phase transformation, segregation, and swelling have all been observed in reactor components. Increases in neutron fluence may exacerbate radiation-induced or -enhanced microstructural and property changes. Comprehensive reviews on radiation effects on the traditional structural materials of LWRs can be found in Ref. [1,2,3].

It is desirable to have advanced alloys that possess greater radiation resistance than the traditional reactor materials. The use of such advanced alloys in replacing the traditional reactor materials for the extension of the existing fleets and the building of new reactors will bring improved safety margins and economics. To identify and develop advanced radiation resistant materials, Electric Power Research Institute (EPRI) has partnered with Department of Energy (DOE) Light Water Reactor Sustainability Program to conduct an Advanced Radiation Resistant Materials (ARRM) program. The EPRI report of "Critical Issues Report and Roadmap for the Advanced Radiation-Resistant Materials Program" [4] reviewed the current commercial and advanced alloys that are applicable as core structural materials of LWRs and laid out a detailed research plan to meet the goal of the program.

High-temperature oxidation resistance in water environment is one of the basic properties required to be screened for the select advanced alloys. Together with other properties such as fracture toughness, radiation-hardening, and irradiation-assisted stress corrosion cracking resistance, the alloys will be down-selected for neutron irradiation study and comprehensive post-irradiation examinations to understand key factors governing superior properties, from which advanced replacement alloys will be developed and recommended for applications in LWR core internals. This report presents the testing results of high-temperature steam oxidation of select advanced replacement alloys.

# 2. MATERIALS AND TEST CONDITIONS

## 2.1 Materials

Table 1 lists fifteen select alloys with respective nominal compositions in weight percentages and heat numbers, which were procured from a variety of vendors or producers. The materials were examined to have acceptable chemistry homogeneity and microstructural uniformity. According to the type of the materials, they are classified as ferritic steels with a body-centered-cubic (bcc) crystal structure, austenitic stainless steels and nickel-base superalloys with a face-centered-cubic (fcc) crystal structure, together with a zirconium alloy, Zr–2.5Nb, with a hexagonal-close-packed (hcp) structure.

**Table 1. Select advanced replacement alloys for high-temperature steam oxidation tests**

| Category | Alloy | Nominal composition | Heat number | Vendor/Producer |
|---|---|---|---|---|
| Ferritic (bcc) | Grade 92 | Fe–9Cr–1.8W–0.5MoVNb | 011448 | Carpenter |
| | 439 | Fe–18Cr | 011438 | Carpenter |
| | 14YWT[*] | Fe–14Cr–3W–TiYO | FCRD-NFA1 | ORNL |
| Austenitic (fcc) | 316L[a] | Fe–16Cr–10Ni–2Mo | 857115 | Outokumpu |
| | 310 | Fe–25Cr–20Ni | 011509 | Carpenter |
| | 800 | Fe–20Cr–32Ni–TiAl | 07032 | Foroni |
| Ni-base (fcc) | 706[b] | 42Ni–37Fe–16Cr–3Nb1.8Ti | 011511 | Carpenter |
| | 718[*,c] | 53Ni–20Cr–17Fe–5.2Nb–3MoTiAl | 399 | Carpenter |
| | 725[*] | 58Ni–22Cr–8Mo–8Fe–4NbTi | 416408 | Carpenter |
| | C22 | 58Ni–22Cr–14Mo–3W–3Fe | 416270 | Carpenter |
| | 625 | 61Ni–22Cr–9Mo–4Nb–4Fe | 602051 | Carpenter |
| | 625DA[*] | 625 direct-aging | JG81 | Allvac |
| | 625-plus[*] | 625+Ti | 215846 | Carpenter |
| | 690 | 60Ni–30Cr–10Fe | NX7075HK11 | Huntington |
| | X-750[*,a] | 71Ni–16Cr–8Fe–2.6TiNbAl | 418365 | Carpenter |
| Others (hcp) | Zr–2.5Nb | Zr-2.5Nb | 251602 | ATI Wah Chang |

[*] High-strength alloys
[a] Reference alloys
[b] Alloy 706 was accidentally added because it was mixed up with Alloy 310 at the beginning of the tests.
[c] Steam oxidation test of Alloy 718 was not conducted because the alloy was procured recently.

There are three ferritic steels, including Grade 92 (a 9Cr ferritic-martensitic steel), Alloy 439 (a 18Cr ferritic stainless steel), and 14YWT [a 14Cr oxide-dispersion-strengthened (ODS) ferritic steel]; three austenitic stainless steels, including 316L, 310, and 800; and eight Ni-base superalloys, including 718, 725, C22, 690, X-750, and three variants of 625. According to their strength, high strength alloys include X-750, 625-plus, 625DA, 725, 718, and 14YWT. The other alloys belong to low-strength alloys. Alloy 706 was accidentally included in the tests because it was mixed up with Alloy 310, both of which were produced into the same form of products in sequence. Because of the later procurement of X-750 and identification of Alloy 310, tests of the two alloys were initiated recently. Among the materials, the steam oxidation test of Alloy 718 was not conducted in this work because the alloy was the last one procured because of the difficulties in finding this type of alloy with acceptable microstructures.

## 2.2 Test Conditions

Coupons in a size of 19 × 10 × 1.5 mm were extracted from the procured alloys for high-temperature steam oxidation tests. The coupons were polished to a 600 grit SiC finish and cleaned ultrasonically in acetone and methanol. Considering the low oxidation rate at the LWR-relevant temperature and the loss-

of-coolant accident scenario, the steam oxidation tests were conducted at elevated temperatures of 600 and 650°C to screen the oxidation resistance of the alloys at the accelerated life testing conditions. Tube furnaces, as shown in Figure 1, were customized for the tests at 1 bar with full steam containing ~10 part-per-billion (ppb) oxygen content. Five coupons per alloy have been tested at 600 and 650°C, respectively, with a targeted exposure time of 5,000 h. The coupons were weighted prior to the exposure and after every 500-h exposure using a Mettler-Toledo model XP205 balance with an accuracy of 0.04 mg or 0.01 mg/cm$^2$. One coupon was taken out of the tests after a total of 500, 1,000, and 2,000 h exposures, respectively, which left two coupons reaching 5,000 h exposures for each alloy at each temperature. The sampling scheme provided reasonable statistics in weight measurements of each alloy. Optical microscopy was employed to characterize the surface morphology and cross-section oxide scales of the exposed coupons that were taken out of the tests.
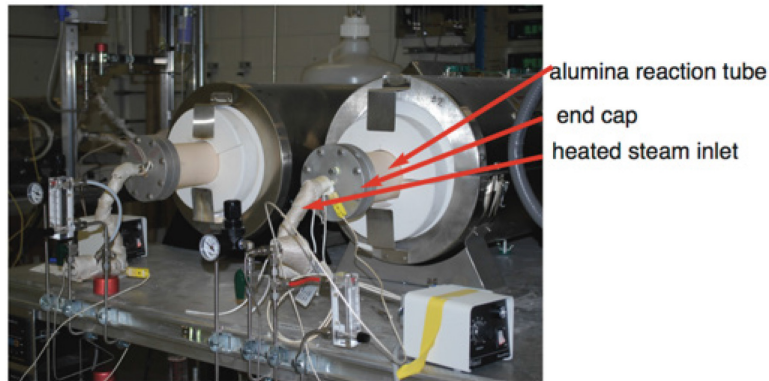


**Figure 1. High-temperature steam oxidation test facility.**

The prepared coupons were arranged in crucibles during the exposure tests. Figure 2 shows an example of 500-h exposed coupons of some alloys at 600 and 650°C. Different colors formed on the coupons due to the specific types of oxides formed on the alloys. The exposed Zr–2.5Nb coupons showed the most distinctive feature as shown for the five coupons at the upper-right corner of Figure 2 at the two temperatures. Photos of the Zr–2.5Nb coupons at a higher magnification in Figure 3 exhibit grainy oxide scales with thick fuzzy oxides at edges after exposure at 600°C, which became severer at 650°C. Consequently, steam oxidation test of Zr–2.5Nb coupons was not continued after the 500-h exposure because of their aggressive oxidation behavior, resulting in exceptional weight gains as shown in Figure 4.



**Figure 2. Photos of the tested alloy coupons in crucibles exposed to steam at 600 and 650°C for 500 h.**
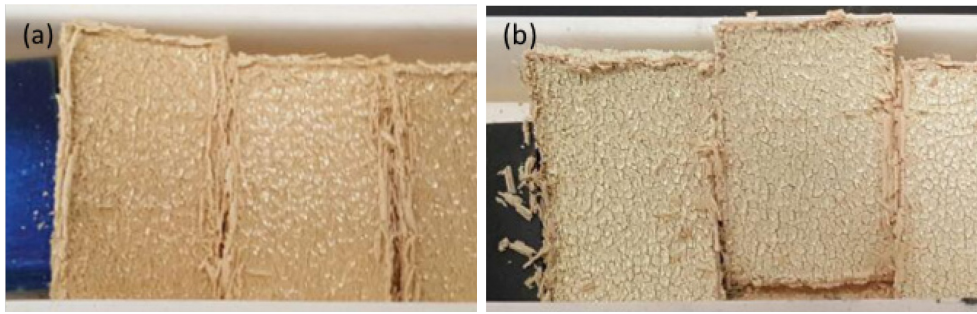
**Figure 3.  Photos of the 500-h exposed Zr–2.5Nb coupons at (a) 600 and (b) 650°C.**

# 3. RESULTS AND DISCUSSIONS

## 3.1 Mass Changes

Mass changes of the ferritic steel coupons of Grade 92, Alloy 439, and 14YWT, together with Zr–2.5Nb, exposed to 1 bar steam at 600 and 650°C are plotted in Figure 4. Each symbol denotes a datum point, with solid symbols and solid fitting lines for the exposed results at 600°C and open symbols and dashed fitting lines for the exposed results at 650°C. Alloy Zr–2.5Nb exhibited exceptional weight gains after 500-h exposure at the two temperatures, which were caused by the extensive oxidation as shown in Figure 3.
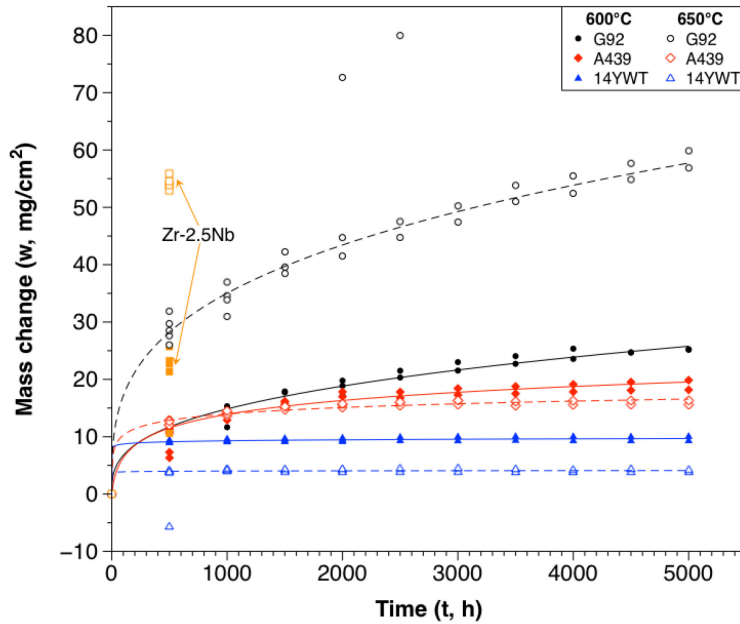


**Figure 4. Mass changes of ferritic steels Grade 92, Alloy 439, and 14YWT, together with Zr–2.5Nb, exposed to 1 bar steam at 600 and 650°C.**

The three ferritic steels showed noticeably weight gains, with Grade 92, Alloy 439, and 14YWT in a descending order. The weight gains of Grade 92 at 650°C were significantly higher than that at 600°C, which were fit well with a function of $w^n = k_1 t$, where $w$ is mass change in mg/cm$^2$, $t$ exposure time in h, $n$ and $k_1$ the fitting mass-change exponent and rate constant, as listed in Table 2 with R$^2$ indicating the goodness of fit. The two data from a coupon of Grade 92 tested at 650°C for 2,000 and 2,500 h had weight gains exceptionally higher than the data of the other coupons at 650°C, which were excluded in the fitting. The cause for such an exceptionally higher weight gains of the coupon is not known yet, which requires detailed comparative microstructural characterization. The fitting results suggest near-cubic oxidation kinetics at both 600 and 650°C. The higher temperature significantly increased rate constant. In contrast to Grade 92, Alloy 439 and 14YWT showed less weight gains at 650°C compared to that at 600°C. The reduced weight gains at the higher temperature were more pronounced for 14YWT compared to Alloy 439. The weight gains of Alloy 439 and 14YWT were fit well with a logarithmic kinetic equation of $w = k_2 \log_{10}(Ct + 1)$ with $k_2$ and $C$ as fitting constants. The fitting results are listed in Table 2. The abnormal weight loss of a 14YWT coupon with 500-h exposure was excluded in the fitting. The lower weight gains of Alloy 439 compared to Grade 92 is attributable to its higher Cr content (18 wt%). However, the 14Cr 14YWT had even lower weight gains than Alloy 439, which suggests that the ultrafine

grains (~0.8 μm) of 14YWT favored grain boundary diffusion as a governing oxidation mechanism. Compared to the oxidation at 600°C, more protective oxide scales were formed on Alloy 439 and 14YWT by the enhanced chromium diffusion at the higher temperature of 650°C to have less weight gains.

**Table 2.  Oxidation kinetics fitting results of Grade 92, Alloy 439, and 14YWT tested at 600 and 650°C**

| Alloy | T (°C) | Fitting equation | $n$ | $k_1$ | $k_2$ | $C$ | $R^2$ |
|---|---|---|---|---|---|---|---|
| G92 | 600 | $w^n = k_1 t$ | 2.917 | 2.612 | | | 0.94 |
| | 650 | | 3.222 | 94.62 | | | 0.96 |
| A439 | 600 | $w = k_2 \log_{10}(Ct + 1)$ | | | 8.147 | 0.04985 | 0.97 |
| | 650 | | | | 3.713 | 5.796 | 0.97 |
| 14YWT | 600 | | | | 0.5662 | $2.551 \times 10^{13}$ | 0.98 |
| | 650 | | | | 0.1320 | $2.266 \times 10^{27}$ | 0.92 |

In contrast to the weight gains of Zr–2.5Nb and the ferritic steels, austenitic stainless steel 316L exhibited the greatest weight losses, which got severer at 650°C to about –60 mg/cm$^2$ as shown in Figure 5. The 316L data fitted by polynomial equations illustrate that the weight losses tend to be stabilized after about 3,000-4,000 h. Alloy 800 exhibited some weight gains, which were lower at 650°C compared to that at 600°C. Alloy 310 only completed 1,000 h exposure, which had slight weight gains comparable to Alloy 800. However, the mass change trends of Alloy 310 are not clear yet.
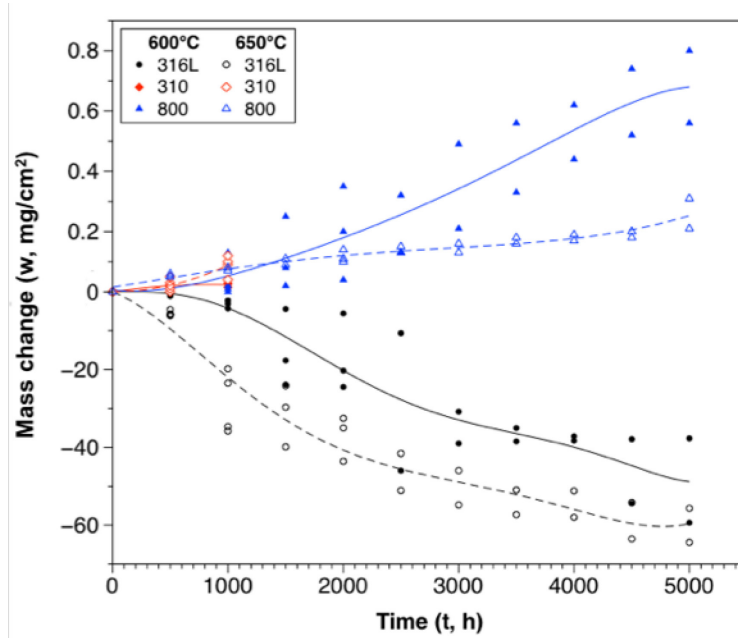


**Figure 5.  Mass changes of austenitic steels 316L, 310 and 800 exposed to 1 bar steam at 600 and 650°C.**

Similarly, Figure 6 shows the mass changes of the exposed coupons of Ni-base superalloys (i.e., X750, 625, 625DA, 625-plus, 690, 725, and C22) at 600 and 650°C. The mass changes of these alloys are much smaller than that of the ferritic steels (Figure 4) and 316L (Figure 5). In contrast to some weight gains of Alloy 800 and 310 (Figure 5), the Ni-base superalloys had slight weight losses at 600°C, but slight weight gains at 650°C. The slight weight gains of the Ni-base superalloys are comparable to that of Alloy 800 at 650°C (Figure 5). Alloy C22 had greater weight losses of up to –0.3 mg/cm$^2$ compared to the similar weight losses (about –0.07 mg/cm$^2$) of the other Ni-base superalloys. The presence of high Mo-

6

content in Alloy C22 (14% Mo) may have increased the weight losses because of the likely formation of volatile molybdenum trioxide ($MoO_3$) deteriorating the integrity of oxide scales.

The Ni-base superalloys had weight gains approximately following parabolic rate kinetics within an exposure period of 4,000 h, after which the weight gains started to decrease. The parabolic growth section at 650°C was fitted with a parabolic rate equation of $w^2 = k_p t$ with $k_p$ as parabolic rate constant. (The other trend lines in Figure 6 were fitted with polynomial equations.) The fitting results of the Ni-base superalloys tested at 650°C are listed in Table 3. Other than Alloy X750 with in-progress tests and the high-Mo Alloy C22 with only up to 2,500 h parabolic growth, the other Ni-base superalloys had up to 4,000 h parabolic growth of their weight gains. According to the fitted parabolic rate constant with higher values for greater weight gains, Alloy 725 and X750 had the greatest and least weight gains, respectively. The oxidation resistance of the Ni-base superalloys in an ascending order at 650°C was Alloy 725, 625-plus, C22, 690, 625DA, 625, and X750 given their small differences in weight gains. Compared to the weight losses at 600°C, the higher temperature at 650°C might have increased the diffusivity of chromium to form protective Cr-rich spinel oxide, favoring the parabolic growth.
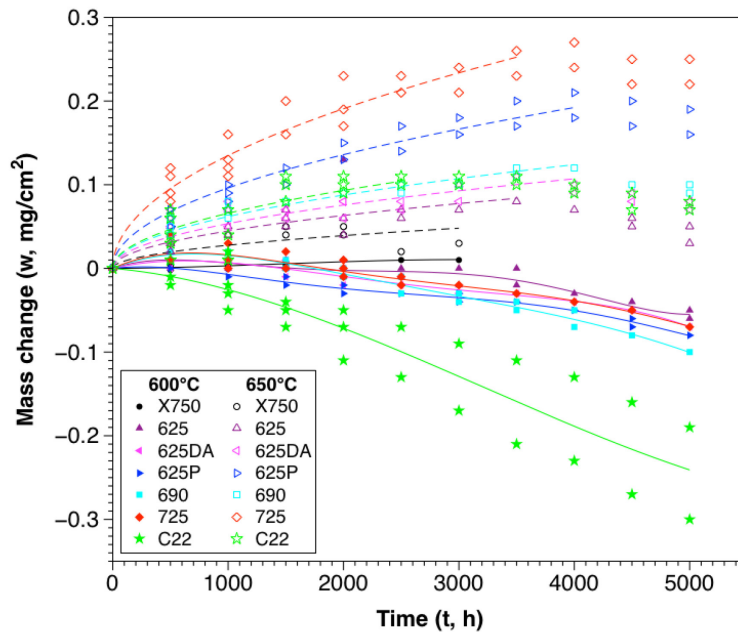


**Figure 6. Mass changes of Ni-base superalloys exposed to 1 bar steam at 600 and 650°C.**

**Table 3. Oxidation kinetics fitting results of Ni-base superalloys tested at 650°C**

| Alloy | Fitting equation | Fitting range (h) | $k_p$ | $R^2$ |
|---|---|---|---|---|
| X750 [*] | | ≤2,000 | $1.495 \times 10^{-6}$ | 0.91 |
| 625 | | ≤3,500 | $2.003 \times 10^{-6}$ | 0.74 |
| 625DA | | ≤4,000 | $2.865 \times 10^{-6}$ | 0.69 |
| 625P | $w^2 = k_p t$ | ≤4,000 | $9.242 \times 10^{-6}$ | 0.95 |
| 690 | | ≤4,000 | $3.843 \times 10^{-6}$ | 0.95 |
| 725 | | ≤3,500 | $1.821 \times 10^{-5}$ | 0.92 |
| C22 | | ≤2,500 | $4.886 \times 10^{-6}$ | 0.81 |

[*] Test is in progress.

## 3.2    Microstructures of Oxide Scales

Surface morphologies of the exposed coupons were imaged using an optical microscope. Figure 7 shows the optical images of one of the two 5,000-h exposed coupons for each ferritic steel tested at 600 and 650°C. Oxide scale exfoliation is noticeable on the Grade 92 coupons. In contrast, the exfoliation on the exposed Alloy 439 and 14YWT coupons is significantly less than that on Grade 92. Similarly, typical surface morphologies of the 5,000-h exposed coupons of austenitic steels (316L and 800) and Ni-base superalloys (625, 625DA, 625-plus, 690, 725, and C22) are shown in Figure 8 and Figure 9, respectively. In contrast to scale exfoliation at some areas at 600°C, nearly all the scales were exfoliated on the 316L at 650°C, which are consistent with their significant weight losses. Oxide exfoliation was not noticeable on Alloy 800 coupons. The uniform darkish surface after exposure at 650°C (Figure 8b) may suggest uniform oxide scale compared with minor exfoliation on Alloy 800 exposed at 600°C. The Ni-base superalloys generally showed brighter surfaces at 600°C compared to the dark surfaces at 650°C, suggesting noticeable oxidation at 650°C.
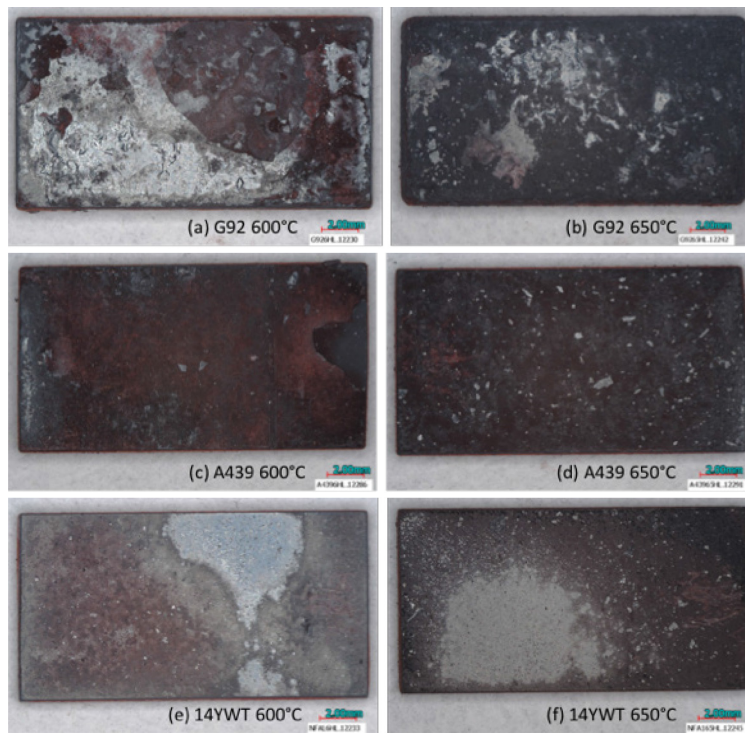


**Figure 7.  Optical images showing the surface morphologies of the 5,000-h exposed coupons of ferritic steels (a,b) Grade 92, (c,d) Alloy 439, and (e,f) 14YWT at 600 and 650°C.**
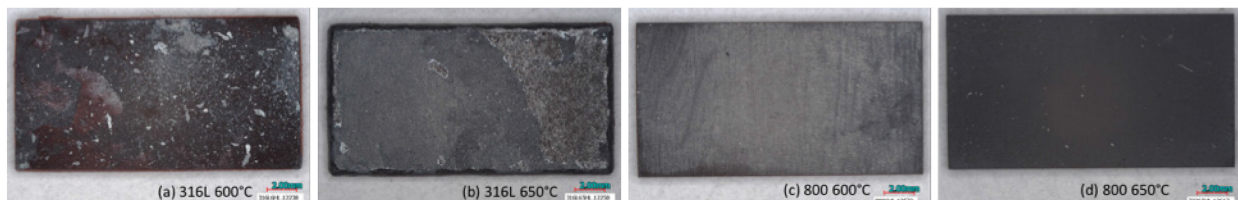


**Figure 8.  Optical images showing the surface morphologies of the 5,000-h exposed coupons of austenitic stainless steels (a,b) 316L and (c,d) Alloy 800 at 600 and 650°C.**
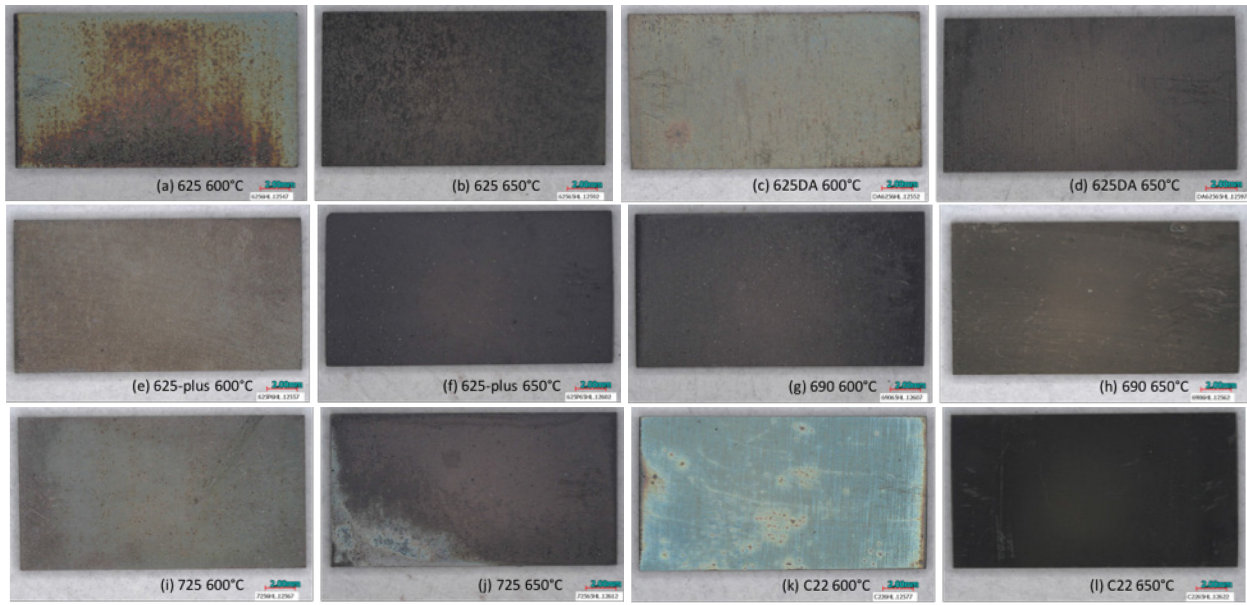
**Figure 9. Optical images showing the surface morphologies of the 5,000-h exposed coupons of Ni-base superalloy (a,b) 625, (c,d) 625DA, (e,f) 625-plus, (g,h) 690, (i,j) 725, and (k,l) C22 at 600 and 650°C.**

Cross-sectional specimens of the 1000-h exposed coupons of ferritic steels Grade 92, Alloy 439, and 14YWT were prepared to characterize the structure of their oxide scales. Cross-sectional specimens of the other alloys were not prepared because of their weight losses or minor weight gains, which would not reveal reliable information of the oxide scales. Figure 10 shows the typical optical images of the oxide scales formed on the ferritic steels. The oxide scale on Grade 92 is primarily composed of two layers at 600°C. Exposure of Grade 92 at 650°C resulted in significant growth of the two layers, together with the formation of an internal oxidation layer at the metal-scale interface and another thin layer at surface. The 650°C exposure also resulted in a continuous gap between the outer-inter-scale interface and coarse cavities in the outer scale on Grade 92, which is distinct from the discrete fine cavities in the outer scale on Grade 92 at 600°C. A three-layer scale structure, including an internal oxidation layer, formed on Alloy 439 and 14YWT at 600°C, which became primarily a two-layer scale structure at 650°C. Similar to Grade 92 but seems less severe, the 650°C exposure resulted in some coarse cavities in the outer scale of Alloy 439 and 14YWT, which tended to result in delamination and exfoliation of the scales.
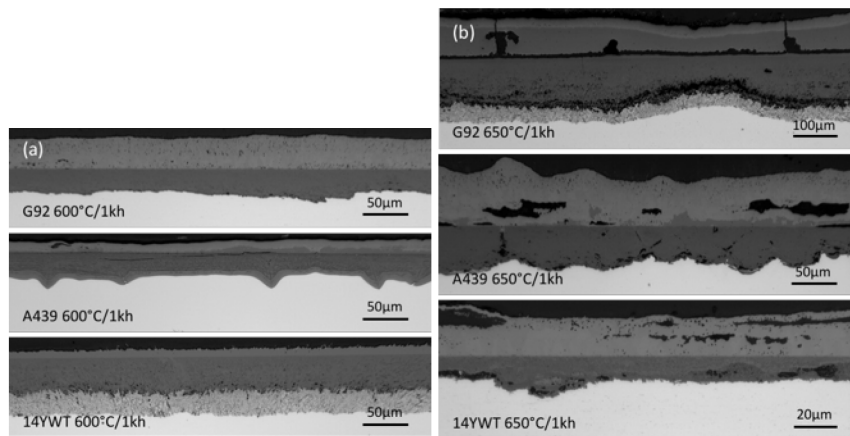


**Figure 10. Optical images of the cross-section oxide scales formed on the 1000-h exposed coupons of ferritic steels Grade 92, Alloy 439, and 14YWT at (a) 600 and (b) 650°C.**

9

The scale thickness of the ferritic steels in Figure 10 is summarized in Table 4. The thickness was averaged by the thin and thick locations of the scale. The ratio of scale thickness at 650°C versus that at 600°C was calculated from the averaged scale thickness. The average weight gain of the samples from Figure 4, together with weight-gain ratio of 650°C versus 600°C, are included Table 4 for comparison. Table 4 indicates that the scale-thickness ratio of Grade 92 and Alloy 439 is significantly larger than their weight-gain ratios, which is believed be attributable to the presence of many large pores or gaps in the outer oxide scales. In contrast, the scale-thickness ratio of 14YWT is comparable to its weight-gain ratio despite the presence of some large pores in its outer oxide scale. Some surface scale exfoliation may have occurred on the 14YWT tested at 600°C because its surface is not as smooth as the other samples in Figure 10. Detailed analysis is needed to understand the changes in oxidation mechanisms at the two temperatures.

**Table 4. Comparison of weight gain and oxide scale thickness of the ferritic steels tested at 600 and 650°C**

| Alloy | T (°C) | Weight-Gain (mg/cm$^2$) | W-G Ratio (650°C/600°C) | Scale-Thickness (μm) | S-T Ratio (650°C/600°C) |
|---|---|---|---|---|---|
| Grade 92 | 600 | 13.95 ± 1.61 | 2.45 ± 0.33 | 66 ± 13 | 3.22 ± 1.07 |
| | 650 | 34.11 ± 2.47 | | 214 ± 58 | |
| Alloy 439 | 600 | 13.80 ± 0.63 | 1.02 ± 0.06 | 45 ± 14 | 2.23 ± 0.91 |
| | 650 | 14.09 ± 0.41 | | 100 ± 26 | |
| 14YWT | 600 | 9.29 ± 0.22 | 0.45 ± 0.02 | 73 ± 6 | 0.44 ± 0.09 |
| | 650 | 4.15 ± 0.19 | | 32 ± 6 | |

### 3.3 Corrosion Rate and Comparison

Corrosion rate (CR) of the alloys was calculated using the equation of *CR* (mm/year) = 87.6$w$/$Dt$, where $w$ is mass change in mg/cm$^2$, $D$ alloy density in g/cm$^3$, and $t$ exposure time of the alloy sample in hours. Figure 11 plots the time-dependent corrosion rate of the tested ferritic steels and austenitic stainless steel 316L. The corrosion rate of the alloys tended to be stabilized with the increasing time, which is independent upon the weight gains of the ferritic steels or weight losses of 316L.
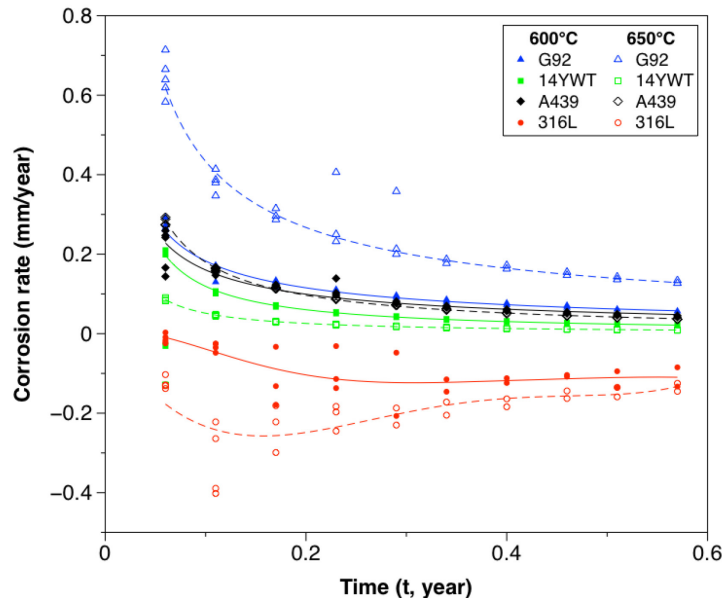


**Figure 11. Corrosion rate of Grade 92, Alloy 439, 14YWT, and 316L tested at 600 and 650°C.**

10

Similarly, the corrosion rate of austenitic stainless steels 800 and 310 and nickel-base superalloys tested at 600 and 650°C is plotted in Figure 12 and Figure 13, respectively. Except for the on-going tests of Alloys 310 and X750, the corrosion rate of the other alloys tended to be stabilized with the increasing time at 600°C. The corrosion rate of Alloy 800 also tended to be stabilized with time at 650°C. However, the corrosion rate of the Ni-base superalloys followed good trends with the parabolic rate law within ≤4,000 h as shown in Figure 6, beyond which their corrosion rates decreased in different levels because of the occurrence of exfoliation.
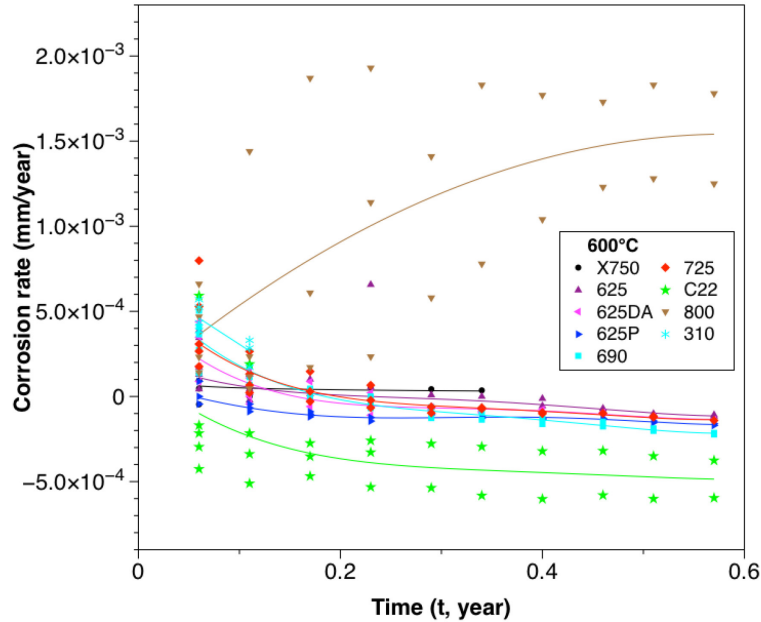


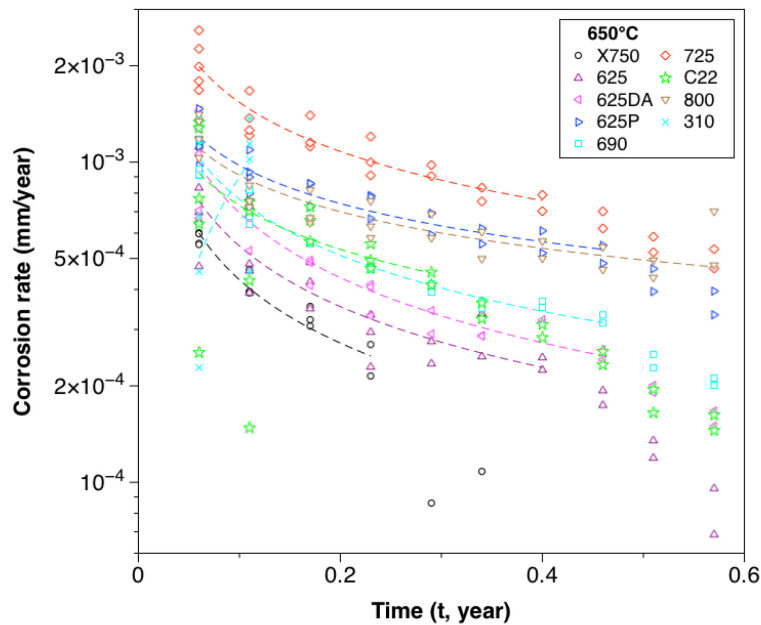**Figure 12. Corrosion rate of Alloys 800 and 310 and Ni-base superalloys tested at 600°C.**



**Figure 13. Corrosion rate of Alloys 800 and 310 and Ni-base superalloys tested at 650°C.**

According to the corrosion rate analysis, the corrosion rate of the alloys tested at 600 and 650°C are plotted in Figure 14 using their longest exposure times for comparison. The bar charts are plotted in blue and red for the weight gains (positive) and weight losses (negative) of the results, respectively. The comparison of the 600°C data in Figure 14a is likely to be more reliable than that of the 650°C data in Figure 14b because of the unstable data of the Ni-base superalloys at the longer exposure times as shown in Figure 13. In general, Zr-2.5Nb had the worst steam oxidation resistance, followed by 316L. The ferritic steels had worse steam oxidation resistance than austenitic stainless steels 310 and 800 and Ni-base superalloys. The Ni-base superalloys exhibited generally comparable steam oxidation resistance. Alloy C22 had relatively worse steam oxidation resistance compared to the other Ni-base superalloys. Alloy X750 tended to have the highest steam oxidation resistance. The on-going tests of Alloy 310 and X750 may slightly change the comparison result.
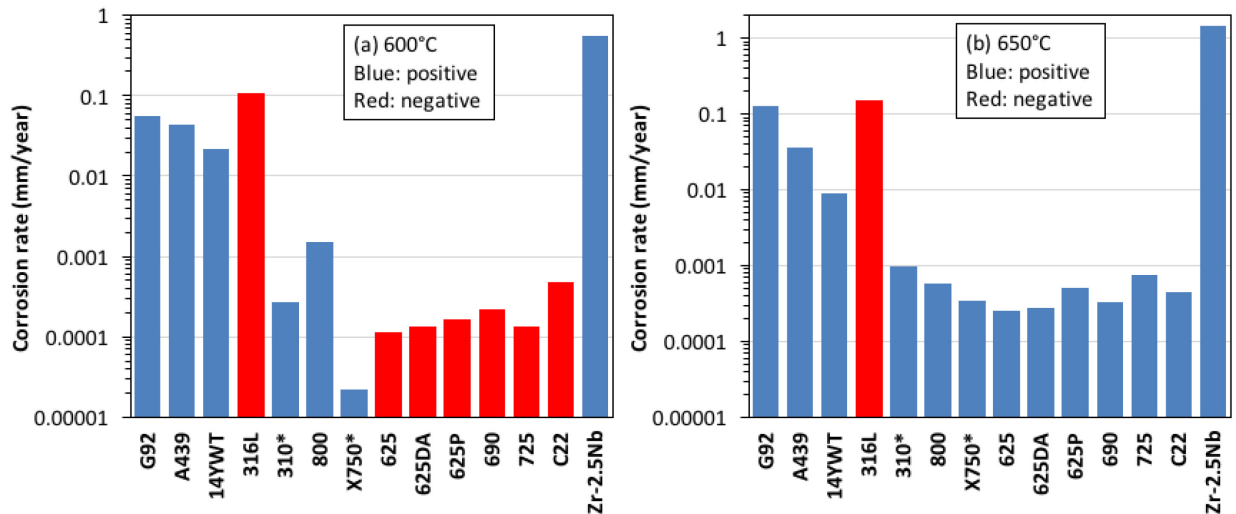


**Figure 14.  Corrosion rate of candidate alloys tested at (a) 600°C and (b) 650°C. (* On-going tests)**

## 3.4    Alloying Effect on Oxidation Resistance

Figure 15 presents the effect of Cr, Ni, and Fe content on the corrosion rate of the alloys tested at 600 and 650°C. The plots suggest that the corrosion rate was significantly reduced with increasing Cr content and when Ni content is above ~15 wt%, but not much further reduced when Fe content is less than ~55 wt%. The on-going test data of Alloys 310 and X750 showed larger deviations from the fitted trend lines compared to the 5,000 h data of the other alloys, which are expected to be diminished as the tests completed at 5,000 h.

**Figure 15.  Effect of (a) Cr, (b) Ni, and (c) Fe content on corrosion rate of the candidate alloys tested at 600 and 650°C.**

### 3.5    Oxidation Thermodynamics of Fe-Cr-O and Fe-Cr-Ni-O Systems

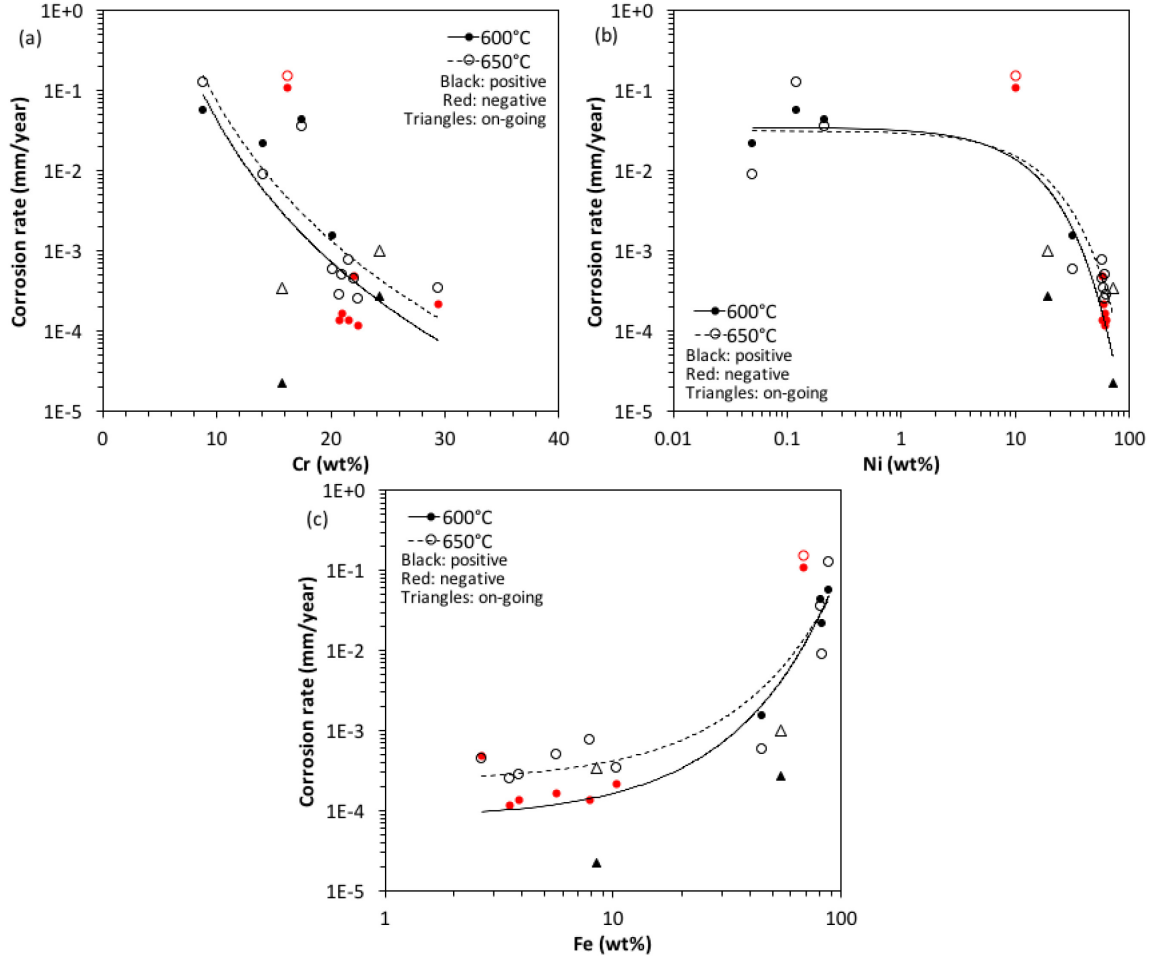Given the noticeable dependence of corrosion rate on the Cr, Ni and Fe content as shown in Figure 15, thermodynamic database of the Fe-Cr-Ni-O system was developed by Dr. Ying Yang of ORNL to understand the oxide scale formation on the tested alloys by calculating oxide stability diagrams. Figure 16 shows the calculated oxide stability diagrams at 650°C for (a) Fe–Cr alloys and (b) $Ni_{80}Cr_{20}$–$Fe_{80}Cr_{20}$ alloys. The oxide stability diagrams at 600°C are not shown here, which have similar layouts as that at 650°C in Figure 16, but generally shifted to lower oxygen partial pressures.

For the ferritic steels Grade 92, Alloy 439, and 14YWT with ~9, ~18, and ~14 wt% Cr, i.e., ~9.5, ~18.5, and ~15.4 mole%, respectively, similar oxide layer structure would form on the steels according to Figure 16a. A Fe-rich hematite [C(H) – $(Fe,Cr)_2O_3$] forms on the surface, followed by Fe-rich magnetite [S(M) – $Fe_2CrO_4$], Fe-rich halite plus Cr-rich spinel [H – (Fe,Cr)O; S – $Cr_2FeO_4$], Cr-rich spinel plus body-centered-cubic (BCC) matrix, and finally Cr-rich corundum [C(C) – $Cr_2O_3$] plus BCC at the oxide-metal interface. The interface between the "H + S" and "BCC + S" is believed to be the initial metal surface prior to the steam exposure, which divides the oxide scales into outer and inner layers. The high Cr of Alloy 439 (~18.5 mole% Cr), as well as the refined-grain of 14YWT with enhanced Cr diffusion by

grain boundary diffusion, favors Cr-rich spinel formation rather than Fe-rich magnetite at outer oxide layer [S(M) + S]. Halite FeO is known for its porosity tendency, resulting in cavities and gaps at the interface of outer-inner oxide layer. Pores also tend to form in Fe-rich magnetite $Fe_2CrO_4$ in the outer layer as elaborated in Ref. [5]. The increased constituent of $Cr_2FeO_4$ in the outer layer of Alloy 439 and 14YWT tends to reduce porosity because it's more protective than $Fe_2CrO_4$ or $Fe_3O_4$ type magnetite.
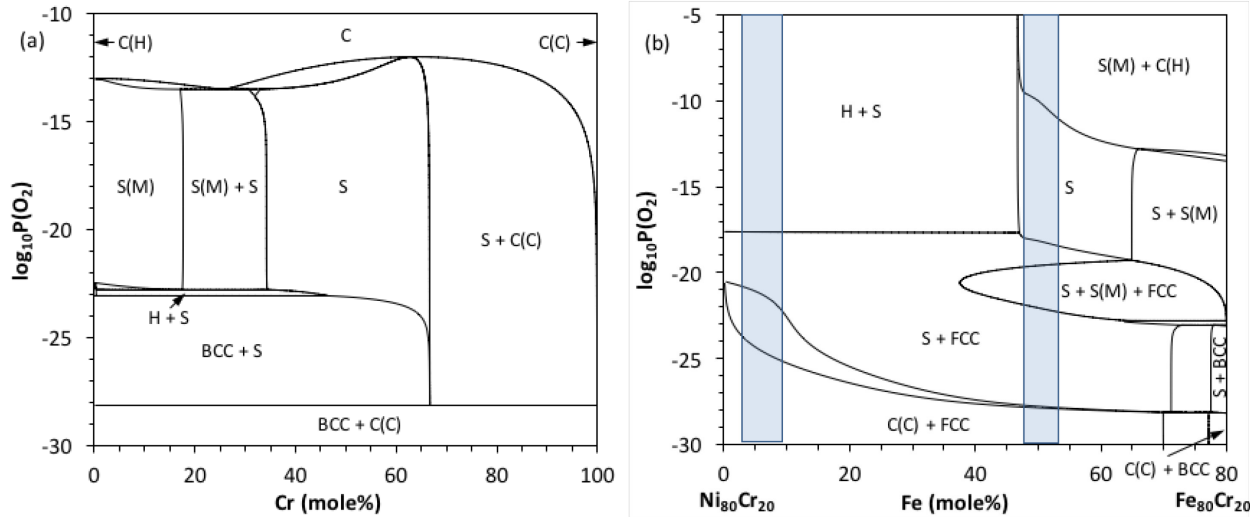


**Figure 16. Calculated equilibrium oxidation of (a) Fe-Cr alloys and (b) Ni$_{80}$Cr$_{20}$-Fe$_{80}$Cr$_{20}$ alloys at 650°C.**

Figure 16b plots the oxide stability diagram of Fe-Cr-Ni ternary alloys with a fixed 20 mole% Cr because of the smaller variation of Cr compared to Ni and Fe, which is used to understand oxidation of austenitic stainless steels 310 and 800 and Ni-base superalloys 725, C22, 625, 625DA, and 625-plus. The same nomenclature as Figure 16a is used for the phases, except for halite (H) as NiO, spinel (S) with Ni involvement, and face-centered-cubic (FCC). The alloys have nominal 20-25 wt% Cr, corresponding to ~21–26 mole% Cr of the alloys. Assuming the 20 mole% Cr calculation would provide indicative results for the tested alloys, the shaded right and left bars approximately represent the compositions of Alloy 800/310 and Ni-base superalloys, respectively. The plot indicates that Alloys 800 and 310 primarily form magnetite and hematite at surface, followed by Ni-involved spinel in the outer oxide layer. In contrast, the outer oxide layer on the Ni-base superalloys is composed of a single layer of NiO plus Ni-involved spinel. Halite NiO is not a protective type of oxide, which tends to cause exfoliation. The inner oxide layer on the Ni-base superalloys is composed of Cr-rich $Cr_2O_3$ and $Cr_2(Fe,Ni)O_4$, which are compact oxide compared to that forms in the inner oxide layer on Alloys 800 and 310.

Detailed thermodynamic evaluation, especially considering some of the major alloying elements such as Mo, coupled with detailed microstructural characterization, is needed to fully understand the oxidation behavior and resistance of the alloys.

# 4. SUMMARY

Coupons from a total of fourteen commercial and custom fabricated alloys were exposed to 1 bar full steam with ~10 ppb oxygen content at 600 and 650°C. The coupons were weighed at 500-h intervals with a total exposure time of 5,000 h. The fourteen alloys are candidate alloys selected under the ARRM program, which include three ferritic steels (Grade 92, 439, and 14YWT), three austenitic stainless steels (316L, 310, and 800), seven Ni-base superalloys (X750, 725, C22, 690, 625, 625 direct-aging, and 625-plus), and one Zr-alloy (Zr–2.5Nb). Among the alloys, 316L and X750 are served as reference alloys for low- and high-strength alloys, respectively. The candidate Ni-base superalloy 718 was procured too late to be included in the tests.

Alloy Zr–2.5Nb was only tested one cycle (500 h) because of the exceptional weight gains and extensive oxide scales formed on the coupons. The tests of 310 and X750 are still in progress because of the later availability of the two alloys. The tests of the other twelve alloys were completed.

Unlike the excessive oxidation of Zr–2.5Nb, ferric steels Grade 92, Alloy 439, and 14YWT showed moderate weight gains in a descending order, which are believed to be primarily determined by their chromium content (9, 18, and 14Cr, respectively) and grain sizes (~40, ~50, and ~0.8 μm, respectively). Oxide scale characterization by optical microscopy revealed pores in the outer oxide layer of the ferritic steels, which caused some scale exfoliation. Significant weight losses with extensive scale exfoliation were observed in 316L. The significantly increased amounts of chromium and nickel in 310, 800, and the Ni-base superalloys led to small or negligible weight changes. Among the Ni-base superalloys, C22 seems to have the worst oxidation resistance, which exhibited the most weight losses at 600°C and unstable weight gains at 650°C, likely attributable to the formation of volatile oxides induced by its high Mo content.

The corrosion rates of the candidate alloys can be approximately interpreted by their Cr, Ni and Fe content. The corrosion rate was significantly reduced with increasing Cr content and when Ni content is above ~15 wt%, but not much further reduced when Fe content is less than ~55 wt% Fe. Simplified thermodynamics analyses of the alloy oxidation provided reasonable indications for the constituents of oxide scales formed on the alloys and explanations for the porosity and exfoliation phenomena because of the nature of specific types of oxides.

# REFERENCES

[1] E.A. Kenik, J.T. Busby, Radiation-induced degradation of stainless steel light water reactor internals, Mater. Sci. Eng. R 73 (2012) 67–83.

[2] F.A. Garner, Radiation damage in austenitic steels, in: R.J.M. Konings, T.R. Allen, R.E. Stoller, S. Yamanaka, Comprehensive Nuclear Materials, Elsevier, The Netherlands, 2012.

[3] L. Tan, R.E. Stoller, K.G. Field, Y. Yang, H. Nam, D. Morgan, B.D. Wirth, M.N. Gussev, J.T. Busby, Microstructural evolution of type 304 and 316 stainless steels under neutron irradiation at LWR relevant conditions, JOM 68 (2016) 517–529.

[4] Critical Issues Report and Roadmap for the Advanced Radiation-Resistant Materials Program, EPRI, Palo Alto, CA and the U.S. Department of Energy, Washington, DC: 2012. 1026482.

[5] L. Tan, Y. Yang, T.R. Allen, Porosity prediction in supercritical water exposed ferritic/martensitic steel HCM12A, Corros. Sci. 48 (2006) 4234–4242.